Title Page

Title: Physical processes in Subglacial Lake Whillans, West Antarctica: inferences from sediment cores

Authors: T.O. Hodson[1], R.D. Powell[1], S.A. Brachfeld[2], S. Tulaczyk[3], R.P. Scherer[1], and the WISSARD Science Team[4]

[1]Department of Geological & Environmental Geosciences, Northern Illinois University, DeKalb, IL, USA
[2]Department of Earth and Environmental Studies, Montclair State University, Montclair, NJ, USA
[3]Department of Earth and Planetary Sciences, University of California, Santa Cruz, California, USA
[4]full list at http://www.wissard.org/about/wissard-personnel

Corresponding author:
T.O. Hodson
Department of Geology and Environmental Geosciences
Northern Illinois University
Davis Hall 312, Normal Rd.
DeKalb, IL 60115
Tel: 1 815 753 1943
e-mail: tohodson@gmail.com

Abstract

The hydrologic system beneath the Antarctic Ice Sheet is thought to influence both the dynamics and distribution of fast flowing ice streams, which discharge most of the ice lost by the ice sheet. Despite considerable interest in understanding this subglacial network and its affect on ice flow, *in situ* observations from the ice sheet bed are exceedingly rare. Here we describe the first sediment cores recovered from an active subglacial lake. The lake, known as Subglacial Lake Whillans, is part of a broader, dynamic hydrologic network beneath the Whillans Ice Stream in West Antarctica. Even though "floods" pass through the lake, the lake floor shows no evidence of erosion or deposition by flowing water. By inference, these floods must have insufficient energy to erode or transport significant volumes of sediment coarser than silt. Consequently, water flow beneath the region is probably incapable of incising continuous channels into the bed and instead follows preexisting subglacial topography. Sediment on the lake floor consists of till deposited during intermittent grounding of the ice stream following flood events. The fabrics within the till are weaker than those thought to develop in thick deforming beds suggesting subglacial sediment fluxes across the ice plain are currently low and unlikely to have a large stabilizing effect on the ice stream's grounding zone.

Text

1. Introduction

Roughly 400 subglacial lakes are currently thought to exist beneath the Antarctic Ice Sheet where its base is at the pressure melting point (Wright and Siegert, 2012). These lakes have generated scientific interest for their potential to harbor unique microbial ecosystems (Christner et al., 2014; Priscu et al., 1999), influence ice dynamics (Bell et al., 2007; Stearns et al., 2008), and preserve paleoclimate or paleoenvironmental records in their sediments (Bentley

et al., 2011). Large deep lakes in the interior, such as Subglacial Lake Vostok, may have existed continuously through the late Cenozoic and potentially contain sedimentary records of the early evolution of the East Antarctic Ice Sheet (Siegert et al., 2001). Other shallower lakes beneath fast flowing ice streams near the ice sheet margin might contain sedimentary records of the dynamic subglacial hydrologic system, which is thought to regulate ice streaming (Anandakrishnan and Alley, 1997). As ice streams discharge 90% of the ice lost from the Antarctic, their dynamics determine the rate at which the ice sheet can affect global sea level (Bamber et al., 2009).

Ice streams occur in zones of low basal drag, where a combination of soft sediments and low effective pressures, the difference between ice overburden pressure and water pressure, act to lubricate the ice sheet bed. As ice stream driving stresses are low, due to their low surface slopes, even small changes within the subglacial hydrologic system can potentially have large effects on basal drag and ice flow (Anandakrishnan and Alley, 1997).

Ice streams are also sensitive to processes at their grounding zones, where they transition to floating ice shelves. When ice streams occur over reverse sloping beds, any retreat places the grounding zone in deeper water where the ice thickness is greater. As the ice flux across the grounding zone increases nonlinearly with ice thickness, this creates a potential for runaway retreat with increasing rates of ice loss (Schoof, 2007; Weertman, 1974). Such a retreat could be triggered by increased melting across the bottom of the ice shelf, thinning the ice and reducing its buttressing effect, or by focused melting at the grounding zone (Rignot and Jacobs, 2002). However, a number of internal mechanisms may counter this instability, including sediment deposition at the grounding zone, which reduces water depth, preventing the ice from going afloat as it thins, and increases the frictional drag from the bed, helping to buttress the ice sheet margin (Alley et al., 2007; Anandakrishnan et al., 2007). Ice stream dynamics therefore reflect a

broad range of processes that integrate glaciology, hydrology, geology, and oceanography (Anandakrishnan et al., 1998; Bindschadler et al., 2003; Clarke, 2005), specifics of which are not well understood, due to the difficulty of accessing and sampling the ice sheet bed. Nevertheless, defining and predicting ice sheet stability requires that we constrain the dynamics of these systems (Joughin et al., 2014; Rignot et al., 2014).

We describe the first sediments recovered from an active Antarctic subglacial lake. The lake, known as Subglacial Lake Whillans (SLW), sits beneath the 800 m thick Whillans Ice Plain (WIP), the lowermost section of the Whillans Ice Stream (WIS) before it goes afloat and flows into the Ross Ice Shelf (Fig. 1a). SLW and other active lakes underlie at least ~10% of this region and were first identified from the short-term fluctuations in the overlying ice surface elevation driven by cyclic draining and filling of the lake waters (Fricker et al., 2007).

From the beginning of satellite altimetric observation in 2004 to our sampling of the lake, SLW had undergone two such fill-and-drain, or "flood", cycles, each lasting approximately two years and separated by quiescent lowstands of more variable duration. When the lake drains, roughly 0.15 km^3 of water discharges over a six-month period, lowering the ice elevation above the lake by ~5 m (Christianson et al., 2012; Fricker et al., 2007). Prior to our sampling in January 2013, the last drainage occurred in 2009, during which ice surface elevations above the lake dropped to ~0.8 m above their lowest observed level (Fig. 1b). Between that drainage and our accessing the lake, the ice surface gradually rose another ~0.6 m, primarily due to dynamic thickening from the slow down of the ice stream (Pritchard et al., 2012; Siegfried et al., 2014).

2. Methods

2.1 Coring Operations

Three coring devices were deployed into SLW: a gravity multi-corer with three 60 mm diameter core barrels designed to recover the soft upper-most sediment and sediment-water interface; a borehole piston corer with a 58 mm diameter core barrel; and a percussion corer with a 10 cm diameter core barrel (Hodgson et al., 2016). Due to a malfunction, percussion-coring was ceased after 10 minutes (approx. 10 blows of the weight). All sediment cores were collected within a 40-hour window, during which time the borehole moved roughly 1m downstream (Tulaczyk et al., 2014). In total, an 80cm long piston core, a 40 cm long percussion core, and six multicores between 20-40 cm long were recovered. Once the sediment cores reached the surface, they were set vertically for at least two days to allow them to outgas and settle before being laid horizontally for packing and refrigerated (4°C) shipping and long-term storage.

2.2 Whole Core Measurements

Sediment cores were split, logged, and sampled at the Hartshorne Quaternary Lab at University of Massachusetts, Amherst. High-resolution line-scan imagery, gamma ray attenuation bulk density and magnetic susceptibility were logged for both whole and split cores using a Geotek multi-sensor core logger. High-resolution ED-XRF spectra were logged on the split cores at a 0.3 mm interval using an ITRAX XRF core scanner, which irradiated the sample with a beam generated from a 3 kW Mo target run at 45 kV and 30 mA over a 15 second exposure time. In addition to line-scan radiographs generated by the ITRAX, high-resolution core radiographs of the split cores were taken using a Torrex 120-D radiograph at Antarctic Marine Geology Research Facility, Florida State University.

2.3 Moisture Content and Particle Size

Sediment moisture content was measured at ~2 – 5 cm intervals by measuring the weight lost after oven drying the sample for 24 hrs at 110°C. Initial wet sample weights ranged between 20 and 50 g. After oven drying, the samples were disaggregated and their particle sizes were analyzed using sieve and pipette methods. As variable clast content in diamicton samples influence measurements of moisture content, the weight of the gravel fraction was subtracted from the bulk weight in determining moisture content. Additional particle size analysis using laser diffractometry was performed at ~10 cm intervals. Approximately 5 g of sediment was gently disaggregated and dry-sieved to remove gravel (>2 mm). An aliquot of the sieved sample was then transferred into a glass bottle with 0.5 ml 5% sodium hexametaphosphate solution and 30 ml deionized water. Samples were then shaken for 8 hours prior to analysis on a Malvern Mastersizer 3000.

2.4 Magnetic Fabric and Magnetic Granulometry

2 cm wide oriented paleomagnetic cubes were collected every 4 – 10 cm along each core for analysis of anisotropy of magnetic susceptibility (AMS) and natural remnant magnetization (NRM). Samples were taken from the center of the cores to avoid disturbance that typically occurs along the outside edge of the core. Unoriented samples were collected at each depth for magnetic granulometry. Stepwise alternating field (AF) demagnetization and measurement of the NRM was performed using a D-tech D-2000 alternating field demagnetizer and AGICO JR-6 spinner magnetometer. Samples were subjected to peak fields of 0 to 80 mT in 5 – 10 mT increments. AMS measurements were made using an AGICO KLY-4 Kappabridge at Montclair State University. The magnetic susceptibility of each cube was measured in 15 orientations, yielding a second-rank susceptibility tensor. The eigenvalues of this tensor are the three principal magnetic susceptibilities, k_{max}, k_{int}, and k_{min}, which represent the lengths of the long, intermediate,

and short axes of a susceptibility ellipsoid. The orientation of each axis (eigenvector) is given by its inclination (*I*) and declination (*D*). Two parameters representing the shape of the AMS ellipsoid are the lineation parameter ($L = k_{max}/k_{min}$), and foliation ($F = k_{int}/k_{min}$). $L < F$ indicates an oblate ellipsoid. $L > F$ indicates a prolate ellipsoid.

AMS fabrics in sediment can arise from the preferential alignment of ferromagnetic and paramagnetic grains during deposition or post-depositional processes, or by coring-induced disturbance. Disturbed portions of the sediment cores were identified by horizontal values of I_{min} and near-vertical values of I_{max} indicating core stretching (Thouveny et al., 2000) or by anomalously high foliation, which can indicate coring-induced compaction.

Magnetic domain state and magnetic mineralogy were determined from hysteresis parameters, thermomagnetic curves, and scanning electron microscopy and energy-dispersive x-ray spectrometry. Hysteresis parameters were measured on bulk sediment using a Princeton Measurements Corp. Vibrating Sample Magnetometer (VSM). Thermomagnetic curves were measured on bulk sediment on an AGICO KLY4 Kappabridge from 20 to 700 ˚C in a flowing argon gas atmosphere. Polished grain mounts were analyzed on a Hitachi S3400N scanning electron microscope equipped with a Bruker X-Flash x-ray microanalysis system.

2.5 Sediment Micromorphology

Sedimentary microfabrics result from the reorientation of sand, silt, and clay grains in response to a deforming stress. Like AMS, microfabrics can help distinguish depositional processes in macroscopically structureless tills. Microfabrics are also susceptible to even small strains (Hiemstra and Rijsdijk, 2003) giving them the potential record disturbance from coring or degassing that may impact NRM and AMS fabrics.

Three 75x35mm sections were extracted from the piston core from shallow (15 – 22.5 cm), intermediate (34 – 42 cm), and deep (67 – 74 cm) intervals and one from the percussion core (23.5 – 31 cm) for micromorphological analysis. The sections were freeze-dried and impregnated with epoxy prior to being cut into thin sections. Each thin section was oriented with respect to vertical but their orientation relative to ice flow is unknown. Microfabrics in the sediments were described following standard terminology used in the glacial literature (i.e., van der Meer, 1993; van der Meer and Menzies, 2011).

2.6 Sediment Lithology

Thin sections made from grain mounts were prepared from size-sorted grains from each phi size fraction between 500 to 2000 μm. Approximately 300 grains in each sample were identified under a petrographic microscope and tallied while making systematic transects across the thin section. The point counts from each size fraction were then aggregated over the 500 – 2000μm range, with each fraction weighted according to the particle size distribution.

3. Results

Sediment cores recovered through the 800 m deep borehole into SLW contain dark grey muddy diamicton, consisting of 8% granules and pebbles, 33% sand, 26% silt and 33% clay, similar to basal sediment sampled ~200 km upstream on the Whillans Ice Stream at a site known as Upstream B (UpB; Tulaczyk et al., 1998). The composition of the sand fraction is indistinguishable from UpB and similar to other samples from the Siple Coast and Eastern Ross Sea Region (Licht et al., 2005). Common lithologies include hydrothermally altered felsic intrusives and meta-sedimentary schists and phyllites. Sedimentary and extrusive rock fragments each constitute ≤1% (Appendix A). With the exception of thin (1 – 2 mm diameter) degassing tubules, the sediment appears structureless. X-radiographs of the cores show variable clast

content with depth but otherwise no discernable stratification or grading (Fig. 2a). High-resolution scans of element chemistry and bulk magnetic susceptibility show negligible stratigraphic variability in chemical and physical properties suggesting the sediment is very homogenous over the sampling depth (~0.8m). Log density also shows no trend despite a logarithmic decrease in moisture content with depth. This difference likely reflects the presence of air filled voids, formed by outgassing as the cores equilibrated to conditions at the surface. Moisture content, which is unaffected by degassing (S. Tulaczyk et al., 2001), is 35% at the sediment-lake water interface. Assuming a compressibility similar to the till upstream (Tulaczyk et al., 2000), this high moisture content implies *in situ* effective stresses during deposition were low (≤1 kPa), similar to the environment inferred to be beneath much of the surrounding ice plain. Sedimentary microfabrics and microstructures within the cores are weakly developed and indicate ductile deformation consistent with shear under low basal effective pressure (e.g., Khatwa and Tulaczyk, 2001; Cowan et al., 2014). Fabric disturbance due to degassing is negligible; however, sections of the cores contain stronger microfabrics associated with coring disturbance that have overprinted the natural fabrics (Appendix B).

The magnetic mineral assemblage in the piston core and percussion core consists of magnetite and ilmenite, possibly with nano-scale hematite intergrowths (Appendix C). However, ilmenite is antiferromagnetic and does not contribute substantially to NRM or AMS signals. Magnetite ranges in size from fine pseudo-single-domain (PSD) to multidomain size, determined from the median destructive field of the NRM (35-40 mT) and from hysteresis loops that are dominated by the multidomain fraction (Appendix C). The magnetic mineral assemblage is uniform throughout PC1 and PEC, consistent with relatively constant Fe/Ti ratios determined from XRF measurements (Fig. 3).

Magnetic fabrics in the cores can be visualized on lower hemisphere, equal-area stereonets, where principal axes of the susceptibility ellipsoid are plotted according to their inclination (analogous to plunge on a stereonet) and declination (analogous to trend). Points that form a tight cluster indicate parallel axes, whereas points that form a great circle represent axes within a common plane. In the piston core, k_{min} axes (red circles) orient vertically, whereas k_{max} axes preferentially orient along a shallow-dipping plane (Fig. 3b). Although partially masked by coring disturbance, the percussion core displays a similar fabric (Appendix B). AMS fabrics in sediment affected only by axial loading, such as coring-induced compaction or natural consolidation, have no preferential azimuthal alignment of k_{int} or k_{max} (Tarling and Hrouda, 1993) indicating the SLW sediment has experienced some degree of horizontal shear.

Natural Remnant Magnetization (NRM) inclinations in the upper 10 cm of the piston core vary around -80˚, consistent with modern International Geomagnetic Reference Field (IGRF) inclinations at the site. Below this depth, inclinations shallow to between -40˚ and -50˚. These deeper samples deviate significantly from the modern paleomagnetic inclination and the geocentric axial dipole value for the site latitude, indicating post-depositional strain, either from consolidation or shear. Samples from the percussion core were uniformly poor recorders of NRM, consistent with coring disturbance inferred from micro- and AMS fabric.

4. Discussion

The access borehole was located over the deepest portion of SLW, which was ~2 m deep in January 2013 (Tulaczyk et al., 2014). At the same time, the average ice elevation above the lake was ~1 m higher than the lowest known level in 2004. After accounting for ~0.6 m of dynamic thickening inferred from altimetry (Pritchard et al., 2012; Siegfried et al., 2014), the ice

stream likely grounded over most of the lake bed in 2004, although a small remnant volume of water may have been present at the drill site.

Structureless diamicton, such as that comprising the lake cores, can form from a number of processes including: rainout through lake waters of debris melted out from basal ice, subaqueous debris flows, or subglacial deformation during periods of grounding (Benn and Evans, 2014; Munro-Stasiuk, 2003). The sheared fabrics within the sediment argue against a rainout origin, and although similar fabrics develop in debris flows, the low gradient and relief of the lake basin makes this mode of deposition highly unlikely (Horgan et al., 2012).

Based on ring-shear experiments on tills, weak fabrics such as those in the SLW sediments indicate low strains. Conversely, under moderate to high strains the maximum susceptibility axes quickly cluster in the shear direction (Hooyer et al., 2008). Iverson (2008) argues that highly clustered, high-strain, fabrics in tills are proof of a thick deforming bed, whereas weaker fabrics are more likely to occur under a more variable strain regime, such as in a thin deforming layer being plowed by protrusions on the ice bed.

Geomagnetic field recording by the surficial sediment does not necessarily conflict with the shear deformation implied by the AMS data. NRM fabrics can reorient to the ambient geomagnetic field under extremely low effective pressure, where the sediment-water mixture approaches its liquid limit. Thus, the same conditions that facilitate ice streaming may also be responsible for preserving NRM fabrics in some tills (Eyles et al., 1987; Gravenor et al., 1973; Stupavsky et al., 1974). NRM ‘lock-in’ depths of two decimeters up to several decimeters are typical for normally consolidated sediments (Snowball et al., 2013; Stoner et al., 2013). The addition of an ice overburden would increase consolidation, reducing the ‘lock-in’ depth; however, given the low effective pressure beneath the ice plain this effect should be small. Based

254 on NRM inclinations in the piston core, 'lock-in' likely occurred at ~10 cm below the sediment-
255 water interface. That inclinations shallow but remain relatively stable below this indicate strains
256 at these depths were low, consistent with the AMS results. Therefore, slip at the ice bed or
257 deformation in the uppermost 10 cm of sediment must accommodate the high strains associated
258 with ice stream flow.

259 Assuming the environment beneath the ice plain is similar to that in the lake basin during
260 grounding events, a shallow deforming bed of the style suggested by the magnetic fabrics would
261 transport <40 m^3 m^{-1} yr^{-1} of till, similar to fluxes estimated much further upstream (Tulaczyk et
262 al., 2001). To arrive at this flux estimate we also assume an ice bed velocity of 350 m/yr and
263 plug flow through a <10 cm thick deforming horizon. In addition, some of the ice motion may be
264 accommodated by basal slip, and strain rates typically decreases with depth across the shear zone
265 (e.g., Hooyer et al., 2008). Thus, the actual till flux may be an order of magnitude lower than our
266 upper estimate. Sediment transported subglacially across the ice plain ultimately accumulates at
267 the grounding zone in the form of a grounding-zone wedge, which can potentially help to
268 stabilize the grounding zone position (Alley et al., 2007). As Antarctic grounding-zone wedges
269 are typically 10-20 km long (Dowdeswell and Fugelli, 2012), this till flux could accumulate a
270 wedge at a rate of <4 mm/yr. Although this accumulation could mitigate the effects of current
271 rates of sea level rise, it might not keep pace with some projections of the late 21st century
272 (IPCC, 2014), and it is orders of magnitude slower than typical melting rates driven by ocean
273 thermal forcing (Rignot and Jacobs, 2002).

274 Despite SLW's history of filling and draining, sediment at and below the modern lakebed
275 shows no evidence of sorting or scour that would indicate a high-velocity water flow. From the
276 empirical Hjulstrom curve for a 1 m-deep flow, mean current velocities in the lake water column

277 likely remain below 20 cm s^{-1} during draining cycles, which is consistent with water fluxes
278 implied by ICESat altimetry (0.15 km^3 over 6 months; Fricker et al., 2007), if the flow pathways
279 are broad. Thus, even though water flows through the subglacial drainage network in "floods"
280 (Fricker and Scambos, 2009), the water has insufficient energy to erode or transport significant
281 volumes of sediment coarser than silt. The dominance of till combined with the lack of stratified
282 sediment or lags on the lake floor suggest sediment fluxes through the hydrologic network
283 upstream and downstream of the lake are low, even relative to the low till flux. By inference,
284 meltwater flow across the central WIP is incapable of incising continuous canals into bed and
285 instead occurs through a more distributed system, maintained, at least in part, by hydrologic
286 jacking where water pressure exceeds that required to float the overlying ice. Thus, the canal
287 imaged by Horgan et al. (2013) crossing the grounding zone downstream of SLW may be a
288 localized feature, possibly eroded by tidal currents or a relic from a time of greater subglacial
289 hydrologic activity.

290 ## 5. Conclusions

291 Although we cannot constrain the last time ice grounded over Subglacial Lake Whillans,
292 the dynamic history of the lake combined with the lack of rainout debris from the actively
293 melting ice above (Fisher et al., 2015), suggest the lacustrine history of the site is short, probably
294 on the order of decades. This subglacial environment is analogous to a non-vegetated wetland
295 within a terrestrial coastal plain, where water bodies tend to be broad and shallow due to the low
296 topographic relief. In the subglacial equivalent, ice may frequently ground following hydrologic
297 adjustments, limiting the long-term persistence of shallow lakes and their sediments. With weak
298 topographic control, frequent avulsions make flow paths dynamic and difficult to predict (e.g.,
299 Carter et al., 2013). Consequently, ice stream subglacial lakes that occur in association with soft

sedimentary beds, as on ice plains, are ephemeral features and poorly preserved in the geologic record, unlike lakes in deep bedrock depressions, such as subglacial lakes Vostok and Ellsworth, which hold greater potential for preserving undisturbed paleoenvironmental archives (Bentley et al., 2011; Filina et al., 2008; Siegert et al., 2001).

Lacustrine sediments beneath SLW were anticipated to provide a longer-term record of the dynamic hydrologic system under this portion of the Antarctic Ice Sheet. Instead we found that the lake was floored by till, which provided insight into the present environment beneath the ice stream, and specifically its ice plain. These regions are likely to have existed over many segments of the ice sheet grounding line during its history and influence both how ice sheets grow and their sensitivity to external climate forcing. Our results suggest that most subglacial sediment transport across the ice plain occurs through a shallow (cm's thick) layer of till with minimal sediment contribution from the subglacial hydrologic network. This low subglacial sediment flux to the Whillans' grounding zone is unlikely to stabilize the grounding zone position against either ocean thermal forcing or changes in ice dynamics and suggests that grounding zones could be more reactive to sea-level rise than previously thought.

Acknowledgements

This work was funded through the NSF (grants ANT-0839107, ANT-0839059, and PLR-1346260). Additional funding for instrumentation development and testing was provided by grants from NOAA (grants NA04OAR4600167 and NA05OAR4311117), Gordon and Betty Moore Foundation, and the Alfred E. Alquist Seismic Saftey Commission of California.

We are grateful to the University of Nebraska-Lincoln drill team and WISSARD traverse personnel, Air National Guard and Kenn Borek Air for their technical and logistical support,

without which this work would not have been possible. We also thank Julie Brigham-Grette for use of the UMass core processing facility, FSU-ARF for taking core x-radiographs, and Rebecca Puttkammer for her help in processing samples.

The manuscript was written by TOH and RDP; SAB conducted measurements of NRM and AMS; TOH described the micromorphology and lithology; and RDP, ST, and RPS contributed to the study design and acquisition of samples.

References

Alley, R.B., Anandakrishnan, S., Dupont, T.K., Parizek, B.R., Pollard, D., 2007. Effect of sedimentation on ice-sheet grounding-line stability. Science 315, 1838–41. doi:10.1126/science.1138396

Anandakrishnan, S., Alley, R.B., 1997. Stagnation of Ice Stream C, West Antarctica by water piracy. Geophys. Res. Lett. 24, 265–268. doi:10.1029/96GL04016

Anandakrishnan, S., Blankenship, D.D., Alley, R.B., Stoffa, P.L., 1998. Influence of subglacial geology on the position of a West Antarctic ice stream from seismic observations. Nature 394.

Anandakrishnan, S., Catania, G. a, Alley, R.B., Horgan, H.J., 2007. Discovery of till deposition at the grounding line of Whillans Ice Stream. Science 315, 1835–8. doi:10.1126/science.1138393

Bamber, J.L., Riva, R.E.M., Vermeersen, B.L. a, LeBrocq, A.M., 2009. Reassessment of the potential sea-level rise from a collapse of the West Antarctic Ice Sheet. Science 324, 901–3. doi:10.1126/science.1169335

Bell, R.E., Studinger, M., Shuman, C. a, Fahnestock, M. a, Joughin, I., 2007. Large subglacial lakes in East Antarctica at the onset of fast-flowing ice streams. Nature 445, 904–7. doi:10.1038/nature05554

Benn, D., Evans, D.J., 2014. Glaciers and Glaciation. Routledge.

Bentley, M.J., Christoffersen, P., Hodgson, D.A., Smith, A.M., Tulaczyk, S., Brocq, A.M. Le, 2011. Subglacial Lake Sediments and Sedimentary Processes : Potential Archives of Ice Sheet Evolution , Past Environmental Change , and the Presence of Life.

Bindschadler, R.A., King, M.A., Alley, R.B., Anandakrishnan, S., Padman, L., 2003. Tidally controlled stick-slip discharge of a West Antarctic ice. Science 301, 1087–1089. doi:10.1126/science.1087231

Carter, S.P., Fricker, H. a., Siegfried, M.R., 2013. Evidence of rapid subglacial water piracy under Whillans Ice Stream, West Antarctica. J. Glaciol. 59, 1147–1162.

355 doi:10.3189/2013JoG13J085

356 Christianson, K., Jacobel, R.W., Horgan, H.J., Anandakrishnan, S., Alley, R.B., 2012. Subglacial
357 Lake Whillans — Ice-penetrating radar and GPS observations of a shallow active reservoir
358 beneath a West Antarctic ice stream. Earth Planet. Sci. Lett. 331-332, 237–245.
359 doi:10.1016/j.epsl.2012.03.013

360 Christner, B.C., Priscu, J.C., Achberger, A.M., Barbante, C., Carter, S.P., Christianson, K.,
361 Michaud, A.B., Mikucki, J.A., Mitchell, A.C., Skidmore, M.L., Vick-Majors, T.J., Adkins,
362 W.P., Anandakrishnan, S., Barcheck, G., Beem, L., Behar, A., Beitch, M., Bolsey, R.,
363 Branecky, C., Edwards, R., Fisher, A., Fricker, H. a., Foley, N., Guthrie, B., Hodson, T.,
364 Jacobel, R., Kelley, S., Mankoff, K.D., McBryan, E., Powell, R., Purcell, A., Sampson, D.,
365 Scherer, R., Sherve, J., Siegfried, M., Tulaczyk, S., 2014. A microbial ecosystem beneath
366 the West Antarctic ice sheet. Nature 512, 310–313. doi:10.1038/nature13667

367 Clarke, G.K.C., 2005. Subglacial Processes. Annu. Rev. Earth Planet. Sci. 33, 247–276.
368 doi:10.1146/annurev.earth.33.092203.122621

369 Cowan, E.A., Christoffersen, P., Powell, R.D., Talarico, F.M., 2014. Dynamics of the late Plio–
370 Pleistocene West Antarctic Ice Sheet documented in subglacial diamictites, AND-1B drill
371 core. Glob. Planet. Change 119, 56–70. doi:10.1016/j.gloplacha.2014.05.011

372 Eyles, N., Day, T.E., Gavican, a., 1987. Depositional controls on the magnetic characteristics of
373 lodgement tills and other glacial diamict facies. Can. J. Earth Sci. 24, 2436–2458.
374 doi:10.1139/e87-229

375 Filina, I.Y., Blankenship, D.D., Thoma, M., Lukin, V. V., Masolov, V.N., Sen, M.K., 2008. New
376 3D bathymetry and sediment distribution in Lake Vostok: Implication for pre-glacial origin
377 and numerical modeling of the internal processes within the lake. Earth Planet. Sci. Lett.
378 276, 106–114. doi:10.1016/j.epsl.2008.09.012

379 Fisher, A.T., Mankoff, K.D., Tulaczyk, S.M., Tyler, S.W., Foley, N., Team, W.S., 2015. High
380 geothermal heat flux measured below the West Antarctic Ice Sheet. Nat. Adv. 1–9.

381 Fricker, H.A., Scambos, T., 2009. Connected subglacial lake activity on lower Mercer and
382 Whillans Ice Streams, West Antarctica, 2003–2008. J. Glaciol. 55, 303–315.
383 doi:10.3189/002214309788608813

384 Fricker, H.A., Scambos, T., Bindschadler, R., Padman, L., 2007. An active subglacial water
385 system in West Antarctica mapped from space. Science 315, 1544–8.
386 doi:10.1126/science.1136897

387 Gravenor, C.P., Stupavsky, M., Symons, D.T.A., 1973. Paleomagnetism and its Relationship to
388 Till Deposition. Can. J. Earth Sci. doi:10.1139/e73-092

389 Hiemstra, J.F., Rijsdijk, K.F., 2003. Observing artificially induced strain: implications for
390 subglacial deformation. J. Quat. Sci. 18, 373–383. doi:10.1002/jqs.769

391 Hodgson, D.A., Bentley, M.J., Smith, A., Klepacki, J., Makinson, K., Smith, M., Saw, K.,
392 Scherer, R., Powell, R., Tulaczyk, S., Rose, M., Pearce, D., Mowlem, M., Keen, P., Siegert,
393 M.J., Hodgson, D.A., 2016. Technologies for retrieving sediment cores in Antarctic
394 subglacial settings Subject Areas : Author for correspondence : Philos. Trans. A. Math.

Phys. Eng. Sci. 374. doi:10.1098/rsta.2015.0056

Hooyer, T.S., Iverson, N.R., Lagroix, F., Thomason, J.F., 2008. Magnetic fabric of sheared till: A strain indicator for evaluating the bed deformation model of glacier flow. J. Geophys. Res. 113, F02002. doi:10.1029/2007JF000757

Horgan, H.J., Alley, R.B., Christianson, K., Jacobel, R.W., Anandakrishnan, S., Muto, A., Beem, L.H., Siegfried, M.R., 2013. Estuaries beneath ice sheets. Geology 41, 1159–1162. doi:10.1130/G34654.1

Horgan, H.J., Anandakrishnan, S., Jacobel, R.W., Christianson, K., Alley, R.B., Heeszel, D.S., Picotti, S., Walter, J.I., 2012. Subglacial Lake Whillans — Seismic observations of a shallow active reservoir beneath a West Antarctic ice stream. Earth Planet. Sci. Lett. 331-332, 201–209. doi:10.1016/j.epsl.2012.02.023

Joughin, I., Smith, B.E., Medley, B., 2014. Marine ice sheet collapse potentially under way for the Thwaites Glacier Basin, West Antarctica. Science 344, 735–8. doi:10.1126/science.1249055

Khatwa, A., Tulaczyk, S., 2001. Microstructural interpretations of modern and Pleistocene subglacially deformed sediments: the relative role of parent material and subglacial processes. J. Quat. Sci. 16, 507–517. doi:10.1002/jqs.609

Licht, K.J., Lederer, J.R., Jeffrey Swope, R., 2005. Provenance of LGM glacial till (sand fraction) across the Ross embayment, Antarctica. Quat. Sci. Rev. 24, 1499–1520. doi:10.1016/j.quascirev.2004.10.017

Munro-Stasiuk, M.J., 2003. Subglacial Lake McGregor, south-central Alberta, Canada. Sediment. Geol. 160, 325–350. doi:10.1016/S0037-0738(03)00090-3

Priscu, J.C., Adams, E.E., Lyons, W.B., Voytek, M. a, Mogk, D.W., Brown, R.L., McKay, C.P., Takacs, C.D., Welch, K. a, Wolf, C.F., Kirshtein, J.D., Avci, R., 1999. Geomicrobiology of subglacial ice above Lake Vostok, Antarctica. Science 286, 2141–2144. doi:10.1126/science.286.5447.2141

Pritchard, H.D., Ligtenberg, S.R.M., Fricker, H. a., Vaughan, D.G., van den Broeke, M.R., Padman, L., 2012. Antarctic ice-sheet loss driven by basal melting of ice shelves. Nature 484, 502–505. doi:10.1038/nature10968

Rignot, E., Jacobs, S.S., 2002. Rapid bottom melting widespread near Antarctic Ice Sheet grounding lines. Science 296, 2020–2023. doi:10.1126/science.1070942

Rignot, E., Mouginot, J., Morlighem, M., Seroussi, H., Scheuchl, B., 2014. Widespread, rapid grounding line retreat of Pine Island, Thwaites, Smith, and Kohler glaciers, West Antarctica, from 1992 to 2011. Geophys. Res. Lett. 41, 3502–3509. doi:10.1002/2014GL060140

Schoof, C., 2007. Marine ice-sheet dynamics. Part 1. The case of rapid sliding. J. Fluid Mech. 573, 27. doi:10.1017/S0022112006003570

Siegert, M.J., Ellis-Evans, J.C., Tranter, M., Mayer, C., Petit, J.R., Salamatin, a, Priscu, J.C., 2001. Physical, chemical and biological processes in Lake Vostok and other Antarctic subglacial lakes. Nature 414, 603–609. doi:10.1038/414603a

435 Siegfried, M.R., Fricker, H.A., Roberts, M., Scambos, T.A., Tulaczyk, S., 2014. A decade of
436 West Antarctic subglacial lake interactions from combined ICESat and CryoSat-2 altimetry.
437 Geophys. Res. Lett. 41, 891–898. doi:10.1002/2013GL058616

438 Snowball, I., Mellström, A., Ahlstrand, E., Haltia, E., Nilsson, A., Ning, W., Muscheler, R.,
439 Brauer, A., 2013. An estimate of post-depositional remanent magnetization lock-in depth in
440 organic rich varved lake sediments. Glob. Planet. Change 110, 264–277.
441 doi:10.1016/j.gloplacha.2013.10.005

442 Stearns, L.A., Smith, B.E., Hamilton, G.S., 2008. Increased flow speed on a large East Antarctic
443 outlet glacier caused by subglacial floods. Nat. Geosci. 1, 827–831. doi:10.1038/ngeo356

444 Stoner, J.S., Channell, J.E.T., Mazaud, A., Strano, S.E., Xuan, C., 2013. The influence of high-
445 latitude flux lobes on the Holocene paleomagnetic record of IODP Site U1305 and the
446 northern North Atlantic. Geochemistry, Geophys. Geosystems 14, 4623–4646.
447 doi:10.1002/ggge.20272

448 Stupavsky, M., Gravenor, C.P., Symons, D.T.A., 1974. Paleomagnetism and magnetic fabric of
449 the Leaside and Sunnybrook Tills near Toronto, Ontario. Bull. Geol. Soc. Am. 85, 1233–
450 1236. doi:10.1130/0016-7606(1974)85<1233:PAMFOT>2.0.CO;2

451 Tarling, D., Hrouda, F., 1993. The Magnetic Anisotropy of Rocks. Chapman and Hall, London.

452 Thouveny, N., Moreno, E., Delanghe, D., Candon, L., Lancelot, Y., Shackleton, N.J., 2000. Rock
453 magnetic detection of distal ice-rafted debries: Clue for the identification of Heinrich layers
454 on the Portuguese margin. Earth Planet. Sci. Lett. 180, 61–75. doi:10.1016/S0012-
455 821X(00)00155-2

456 Tulaczyk, S., Kamb, B., Engelhardt, H.F., 2001. Estimates of effective stress beneath a modern
457 West Antarctic ice stream from till preconsolidation and void ratio. Boreas 30, 101–114.
458 doi:10.1080/030094801750203134

459 Tulaczyk, S., Kamb, B., Engelhardt, H.F., 2000. Basal mechanics of Ice Stream B, West
460 Antarctica: 1. Till mechanics. J. Geophys. Res. Solid Earth 105, 463–481.

461 Tulaczyk, S., Kamb, B., Scherer, R.P., Engelhardt, H.F., 1998. Sedimentary processes at the base
462 of a West Antarctic ice stream: constraints from textural and compositional properties of
463 subglacial debris. J. Sediment. Res. 68, 487–496.

464 Tulaczyk, S., Mikucki, J. a., Siegfried, M.R., Priscu, J.C., Barcheck, C.G., Beem, L.H., Behar,
465 A., Burnett, J., Christner, B.C., Fisher, A.T., Fricker, H. a., Mankoff, K.D., Powell, R.D.,
466 Rack, F., Sampson, D., Scherer, R.P., Schwartz, S.Y., 2014. WISSARD at Subglacial Lake
467 Whillans, West Antarctica: scientific operations and initial observations. Ann. Glaciol. 55,
468 51–58. doi:10.3189/2014AoG65A009

469 Tulaczyk, S.M., Scherer, R.P., Clark, C.D., 2001. A ploughing model for the origin of weak tills
470 beneath ice streams: a qualitative treatment. Quat. Int. 86, 59–70. doi:10.1016/S1040-
471 6182(01)00050-7

472 van der Meer, J.J., 1993. Microscopic evidence of subglacial deformation. Quat. Sci. Rev. 12,
473 553–587.

474 van der Meer, J.J.M., Menzies, J., 2011. The micromorphology of unconsolidated sediments.

Sediment. Geol. 238, 213–232. doi:10.1016/j.sedgeo.2011.04.013

Weertman, J., 1974. Stability of the junction of an ice sheet and an ice shelf. J. Glaciol. 13, 3–11.

Wright, A., Siegert, M., 2012. A fourth inventory of Antarctic subglacial lakes. Antarct. Sci. 24, 1–6. doi:10.1017/S095410201200048X

Figures

Figure 1. a) Location of the WIS and SLW [from *Christner et al.*, 2014b]. The maximum extent of SLW and other subglacial lakes in blue; predicted subglacial water flowpaths through SLW and other subglacial lakes are represented by blue lines with arrows; the black line denotes the ice-sheet grounding line at the start of the Ross Ice Shelf. Inset shows details of SLW with both maximum (solid blue line) and minimum lake extent (shaded blue area), hydropotential contours (white isolines; 25 kPa interval), and drill site (yellow star; 84.240° S 153.694° W). Background imagery is MODIS MOA30. **b)** Relative change in average lake surface elevation between 2004 and 2014 (Siegfried et al., 2014).

Figure 2. a) Right to left: Geotek line-scan images of piston core (SLW1-PC1), core radiograph, digitized clasts, moisture content, Geotek wet bulk density, and ITRAX Fe:Ti. **b)** Particle size distribution of till matrix, measured by laser diffraction. The mean and 2-sigma distributions are shown by the solid line and shaded region, respectively.

Figure 3. AMS fabric in the piston core (left column) and percussion core (right column). **a)** Plots showing the variation in lineation ($L = k_{max}/k_{min}$) and foliation ($F = k_{int}/k_{min}$) versus depth in the piston and percussion cores respectively. Vectors represent the magnitude and inclination of the k_{min} principle susceptibility axis. **b)** Maximum (squares), intermediate (triangles), and minimum (circles) principal susceptibilities with disturbed sections omitted to highlight the natural fabric. k_{max} orientations trend towards a shallow plane depicted by the blue line. As the cores are not azimuthally oriented, the three principal susceptibility axes have been rotated by a

504 constant so that the k_{min} axes plunge eastward or 'down-glacier', consistent with experimental
505 observations from sheared diamict (Hooyer et al., 2008).

506 Appendix A. Sand Mineralogy

507 Composition of the sand fraction at SLW is statistically indistinguishable from sediments
508 recovered upstream (at UpB) and very similar to previously described samples from the Siple
509 Coast and Eastern Ross Sea Region (Licht et al., 2005). In order of decreasing abundance, the
510 500 – 2000μm size fraction contained quartz (37%), feldspar (24%), felsic intrusive lithic
511 fragments (19%), metamorphic lithic fragments (14%), and intermediate intrusive lithic
512 fragments (3%). Sedimentary lithic fragments, extrusive lithic fragments, heavy minerals and
513 mafic intrusive lithic fragments each constitute ≤1% (Fig. S1). Felsic intrusive grains commonly
514 display evidence of hydrothermal alteration, either by chlorite replacement of biotite or
515 seritization of feldspars grains. Metamorphic grains are dominantly schists and phyllites, and
516 sedimentary lithics include diamictites, mudstones, limestone, and dolomite.

517 Appendix B. Microfacbrics

518 Microfabrics support this interpretation showing structures consistent with ductile shear
519 and very little disturbance from degassing. Skel-insepic intergrading to skel-lattisepic plasmic
520 fabrics and rotational microstructures are dominant in all of the sampled intervals. Large (0.1 –
521 0.5 mm wide) planar fractures are abundant in the shallowest piston core and percussion core
522 thin sections. In the piston core sample, fractures display a polygonal pattern suggesting they
523 formed by desiccation. Samples used in AMS and NRM were taken immediately after the cores
524 were split and should not have been affected. In the percussion core sample, fractures are
525 dominantly subhorizontal and may have formed from dilation and pressure release caused by the

526 'hammering' of the corer. Planar plasmic fabrics occur in proximity to the fractures where they
527 are aligned parallel to the dominant fracture orientation. We interpret these fabrics as evidence of
528 coring disturbance, which may overprint natural magnetic fabrics in the percussion core.
529 Subvertical planar fabrics occur in the deepest piston core sample (see masepic fabric in Figure
530 S2). The corresponding AMS fabrics have an anomalous vertical trend interpreted as evidence of
531 core stretching (see horizontal K_{min} vectors in Fig. 3a). Degassing tubules tend to be very fine
532 (<0.1 mm wide), rare (<2% of area), and most importantly show very limited disturbance of the
533 surrounding fabric suggesting that degassing has not significantly affected magnetic fabrics in
534 the cores.

535 # Appendix C. Magnetic Granulometry

536 ## 6. Methods

537 The hysteresis parameters saturation magnetization, saturation remanence, coercivity,
538 coercivity of remanence, and high-field magnetic susceptibility (M_S, M_R, B_C, B_{CR}, and χ_{hf},
539 respectively), were measured on a Princeton Measurements Corp. Vibrating Sample
540 Magnetometer (VSM) in a 1-T peak field. Measurements were made on bulk sediment to assess
541 the average domain state responsible for the natural remanent magnetization and anisotropy of
542 magnetic susceptibility behavior. Raw hysteresis data were processed by using χ_{HF} (calculated
543 between 0.7 T and 1 T) to remove the paramagnetic contribution to the induced magnetization,
544 and then normalized by mass. The hysteresis parameters saturation magnetization (M_S),
545 saturation remanence (M_R) and coercivity (H_C) were determined from the paramagnetic-
546 corrected data. The coercivity of remanence (H_{CR}) was determined through the DC-
547 demagnetization of a saturation isothermal remanent magnetization imparted in a 1 T field. The

S-ratio was measured by imparting a 1 T isothermal remanent magnetization, followed by the application of a 300 mT backfield, and calculating S as $M_{R(-300\text{-}mT)}/M_{R(1\text{-}T)}$.

Thermomagnetic curves were measured on an AGICO KLY-4 Kappabridge at Montclair State University. Magnetic susceptibility was measured on a sample size of 500-600 mg of dry sediment during heating and cooling from 20 - 700 ˚C in a flowing argon gas atmosphere. Raw data were corrected for the furnace contribution and normalized by mass.

Grain mounts were prepared to observe Fe-oxide mineral assemblages via electron microscopy following Darby and Bischof, 1996. The 45-500 μm size fraction was wet sieved and then processed using a Franz magnetic separator. The magnetic fraction was examined under an Olympus SZ12 stereomicroscope. Grains with metallic luster were manually picked from the magnetic fraction, mounted in epoxy, polished, and carbon-coated. Polished specimens were examined using a Hitachi S-3400N Scanning Electron Microscope (SEM) equipped with a Bruker X-flash X-ray microanalysis system. Standardless quantitative analysis was performed using the Phi-Rho-Z standardless quantitative analysis routine in Bruker's Esprit 1.9.3 software. Tests of the Phi-Rho-Z routine on microprobe quality mineral standards yielded results within 0.05 to 1% relative of the published compositions for major elements (wt% > 5%) and within 0.05-0.5% relative for minor elements (<5 wt%).

7. Results

The magnetic mineral assemblage in SLW-1 PC1 and PEC-1 is comprised of magnetite and minor amounts of ilmenite and hematite, with the latter likely occurring as nanno-scale lamellae in (hemo)ilmenite. The magnetic mineral assemblage is uniform throughout PC1, consistent with relatively constant Fe/Ti ratios determined from XRF measurements (Fig. 2).

Magnetic domain state was determined from the median destructive field of the NRM (MDF_{NRM}), the alternating field value at which 50% of the NRM is removed, and from hysteresis measurements. MDF_{NRM} values in PC1 are between 35-40 mT, consistent with fine PSD magnetite. Hysteresis parameters in bulk samples from SLW-1 piston core 1 (PC1) and percussion core 1 (PEC-1) are dominated by multidomain grains, with M_R/M_S values between 0.04 and 0.06 and B_{cr}/B_c values between 5 and 6 (Table S1; Figure S4). This is consistent with lithic fragment abundances, for which felsic and intermediate intrusive fragments (i.e, coarse grained lithologies) are abundant, and extrusive fragments (fine grained lithologies) comprise < 1% of the assemblage (Appendix A).

Magnetic mineralogy was determined from thermomagnetic curves, S-ratios, and energy-dispersive x-ray spectroscopy (EDX). S-ratios are nearly 1 for all samples (Table S1), indicative of low coercivity minerals such as magnetite. Susceptibility vs. temperature is invariant between 20 and 380 ˚C. Susceptibility increases between 380 and 450 ˚C, which is likely a thermochemical alteration feature. This is followed by rapid loss of signal between 565 ˚C and 610 ˚C, indicative of low-Ti titanomagnetite and magnetite that are slightly oxidized (Figure S4). A continued loss of signal is observed between 600 and 700 ˚C, which is suggestive of hematite. This feature is reversible in the heating and cooling curves. As no hematite grains were observed in the SEM and the S-ratios are uniformly near 1, we infer this high-temperature signal as originating from nanno-scale hematite intergrowths within ilmenite. SEM and EDX data support the thermomagnetic data. Observations of magnetic grains extracted from the 45-500 μm fraction reveal homogeneous magnetite (72% wt % Fe and no other detectable cations) and homogenous ilmenite in which the Fe wt% (38 %) is very slightly enriched above the stoichiometric value (36.8%).

8. References

Darby, D. A., J.F. Bischof, (1996), A statistical approach to source determination of lithic and Fe-oxide grains: An example from the Alpha Ridge, Arctic Ocean. *J. Sedimentary Res. 66*, 599–607.

Day, R., M.D. Fuller, V.A. Schmidt, (1977), Hysteresis properties of titanomagnetites: Grain size and composition dependence. *Phys. Earth Planet. Int., 13*, 260-266, doi:10.1016/0031-9201(77)90108-X.

Figure 1

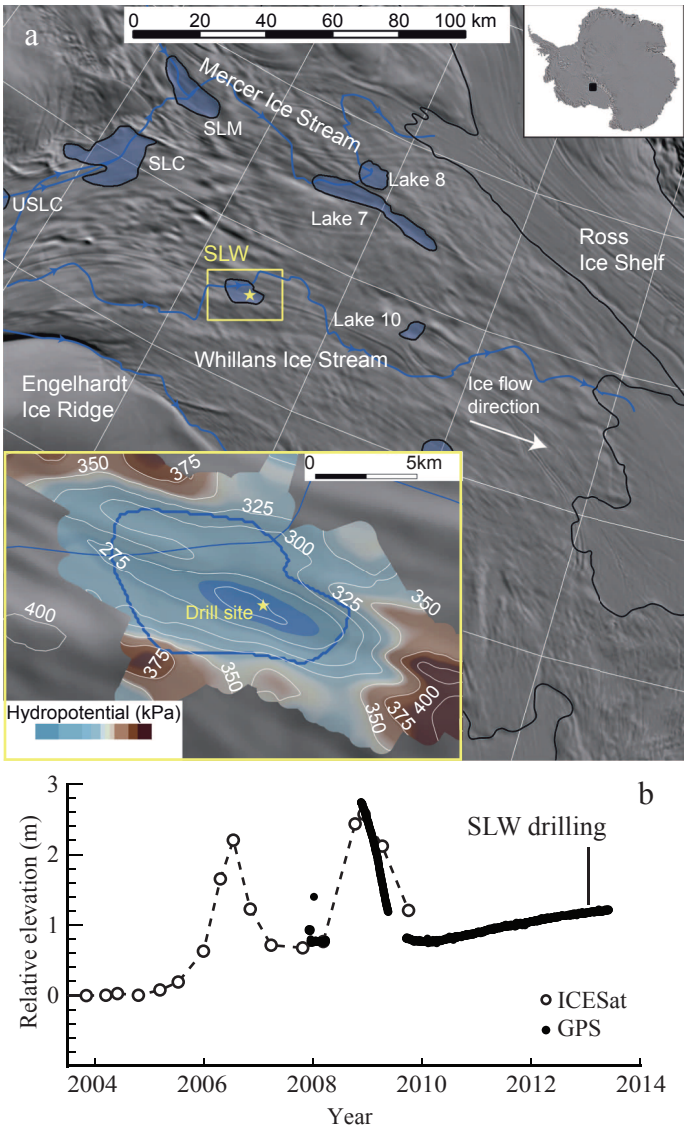
a
0 20 40 60 80 100 km
Mercer Ice Stream
SLM
SLC
USLC
Lake 8
Lake 7
SLW
Lake 10
Ross
Ice Shelf
Whillans Ice Stream
Engelhardt
Ice Ridge
Ice flow
direction
0 5km
350
375
325
300
275
400
Drill site
Hydropotential (kPa)
b
SLW drilling
Relative elevation (m)
ICESat
GPS
2004
2006
2008
2010
2012
2014
Year

Figure 2

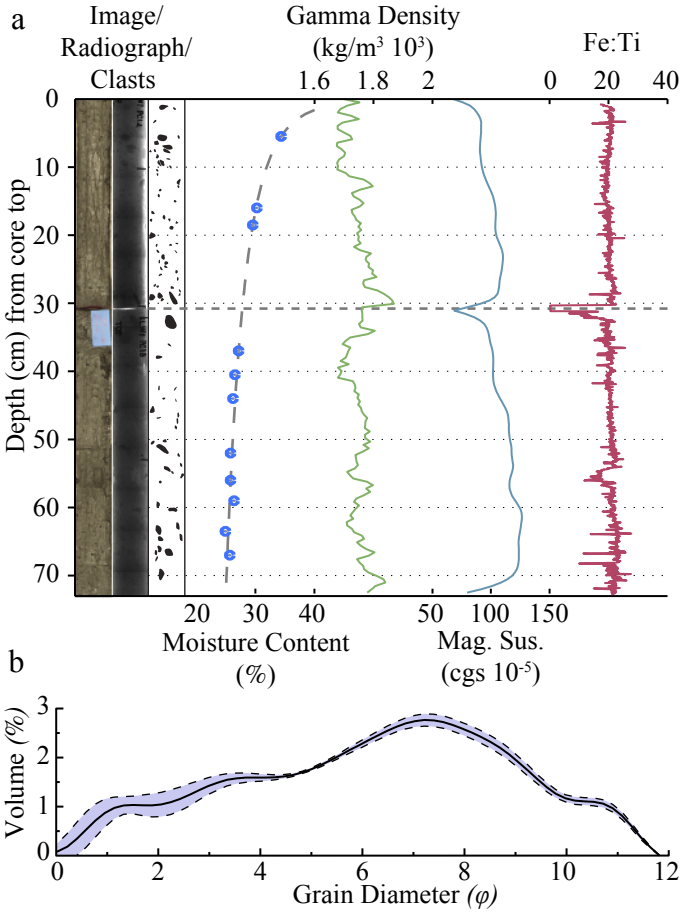
a
Image/
Radiograph/
Clasts
Gamma Density
(kg/m³ 10³)
1.6 1.8 2
Fe:Ti
0 20 40
0
10
20
30
40
50
60
70
Depth (cm) from core top
20 30 40
Moisture Content
(%)
50 100 150
Mag. Sus.
(cgs 10⁻⁵)
b
Volume (%)
0
1
2
3
0 2 4 6 8 10 12
Grain Diameter (φ)

Figure 3

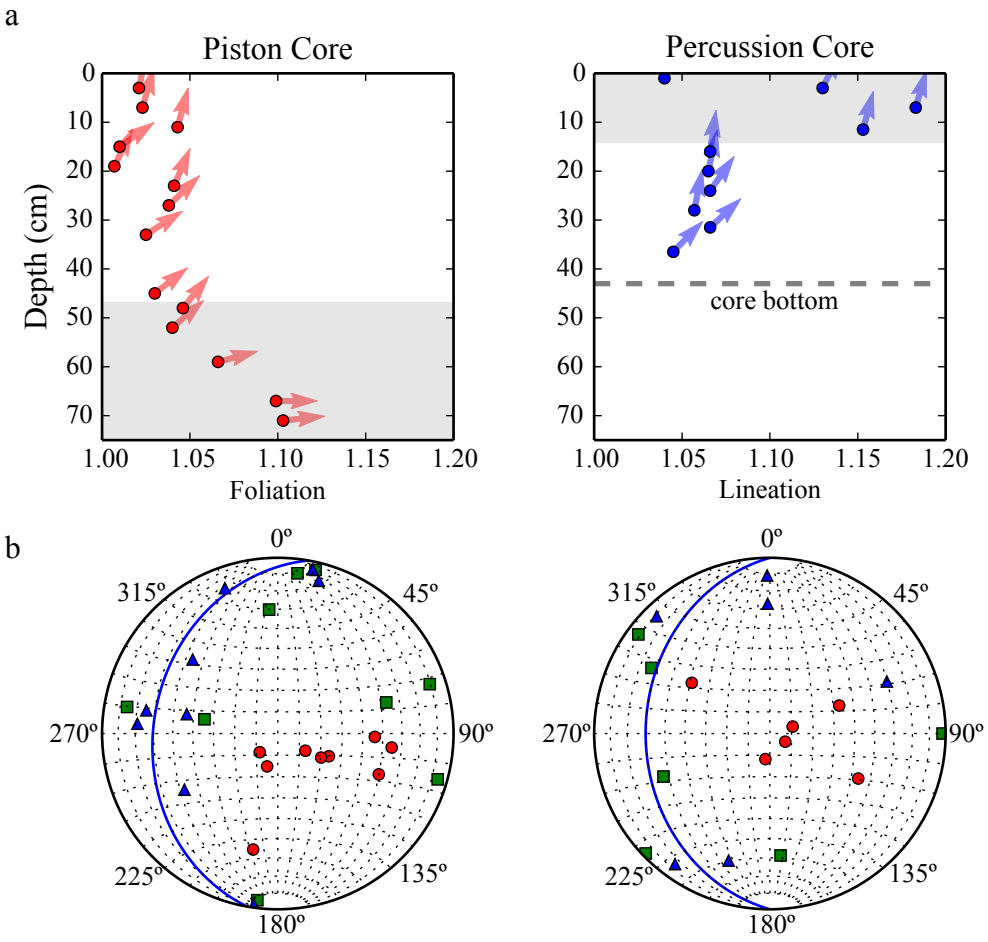
a
Piston Core
Percussion Core
Depth (cm)
0
10
20
30
40
50
60
70
1.00
1.05
1.10
1.15
1.20
Foliation
Lineation
core bottom
b
0º
45º
90º
135º
180º
225º
270º
315º